Available online at www.sciencedirect.com

ScienceDirect

Procedia CIRP 68 (2018) 28 – 33

www.elsevier.com/locate/procedia

19th CIRP Conference on Electro Physical and Chemical Machining, 23-27 April 2018, Bilbao, Spain

Modelling and characterisation of electrical discharge TiC-Fe cermet coatings

Samer J Algodi[a,d], James W Murray[a], Adam T Clare[a,b*], and Paul D Brown[a,c]

[a]*Department of Mechanical, Materials and Manufacturing Engineering; University of Nottingham, University Park, Nottingham, NG7 2RD, UK*

[b]*Institute of Advanced Manufacturing, Faculty of Engineering; University of Nottingham, University Park, Nottingham, NG7 2RD, UK*

[c]Nanoscale and Microscale Research Centre; University of Nottingham, University Park, Nottingham, NG7 2RD, UK

[d] Department of Mechanical Engineering, College of Engineering, Al-Nahrain University, Baghdad, Iraq

* Adam T Clare. Tel.: +115-951-4109; fax: +115-951-3800. E-mail address: adam.clare@nottingham.ac.uk

Abstract

The creation of coatings via Electrical Discharge (ED) methods can enhance the functionality of components which are subject to prior ED machining process steps. However, the industrial application of these methods has been limited due to poor understanding of the fundamental interaction between energy source and material. In this paper, for the case of a TiC sacrificial electrode deposited onto a stainless steel, 2D transient heat transfer is modelled and solved by a finite difference method to estimate the effective fraction of total energy transferred to the workpiece, as well as heat distribution and expected microstructure upon ED coating (EDC). The model was validated via comparison with experimental data, as well as data in literature. In addition, a TiC coating was tested under dry sliding wear conditions to evaluate its tribological properties against an Al_2O_3 counter face sphere using ball-on-flat geometry. The effective amount of energy transferred to the workpiece is predicted to vary between 17% and 23% for increasing current, from 2 to 19 A, at fixed pulse-on time of 8 µs; and between 7% and 53% for increasing pulse-on time, from 2 to 64 µs, at fixed current of 10 A. Backscattered electron (BSE) imaging showed that the coatings comprised a metal matrix composite, with a complex banded fine-grained microstructure and different cooling rate across the coating. A TiC-based ED coating on 304 stainless steel (304-SS) yielded a wear rate two orders of magnitude lower than that of the substrate only.

Peer-review under responsibility of the scientific committee of the 19th CIRP Conference on Electro Physical and Chemical Machining

Keywords: Electrical discharge coating; finite difference method; TiC-Fe cermet; tribology.

1. Introduction

Electrical discharge coating (EDC), an adaptation of electrical discharge machining (EDM), can be used to produce hard coatings. A series of high frequency localised sparks result in melt pool formations and the intermixing of tool electrode with substrate material (Figure 1) [1, 2]. Multiple sparking events allow a large number of overlapping craters to form a continuous coating across the workpiece. During conventional EDM, the removal of material is based on the conversion of electrical energy into thermal energy over a localised area [3]. The energy distribution into the workpiece depends on its physical properties, with the assumption that all electrical energy is turned into heat [4].

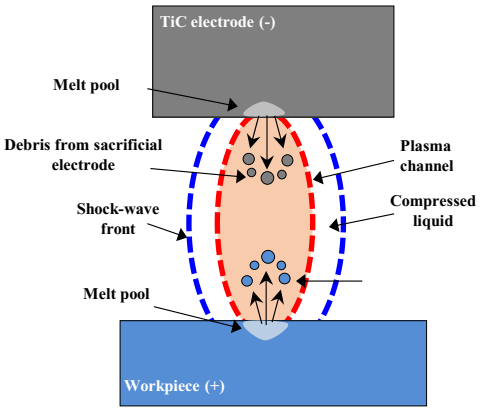

Fig. 1. Schematic representation of the EDC mechanism.

Peer-review under responsibility of the scientific committee of the 19th CIRP Conference on Electro Physical and Chemical Machining
doi:10.1016/j.procir.2017.12.017

A number of models have been developed for the EDM process, based on electro-thermal or electro-mechanical mechanisms of material removal [5], using analytical or numerical solutions. Effective methods have been reported for calculating temperature distributions and crater geometries, and for estimating amounts of material removed, based on single spark events and heat transfer equations. For example, a comprehensive comparison by Yeo *et al.* [6] of five different electro-thermal models, considering temperature distribution, crater geometry and material removal rate, demonstrated that the model of Di Bitonto *et al.* [7], which assumed that only 18% of the energy was transferred to the cathode, showed better agreement with experimental data than if it were assumed that 50% of the energy was transferred, which led to an overestimate of workpiece temperature and the size of the resultant craters.

In the present work, a model is presented which provides for estimation of the amount of energy transferred to the workpiece, along with predictions for crater geometry and microstructure development in EDC during cool down. We use the model, backed up by experimental data, to describe the fundamentals of the EDC processing of cermet layers, using a semi-sintered TiC tool electrode and a 304-SS substrate. Additionally, the dry sliding wear behaviour of cermet coatings is tested and compared with simple EDM surfaces processed using a standard Cu tool electrode, and explained with reference to the developed cermet microstructural properties.

2. Process modelling and simulation

A two dimensional, axi-symmetric, transient heat transfer model, using a finite difference method, has been developed. This allows for electro-thermal heating to be determined, for a single discharge event incident upon a workpiece surface. The domain was defined with dimensions 3 x 1.5 times the crater radius, in x and y directions, respectively; with a uniform square mesh of grid spacing $\Delta x = \Delta y = 0.5$ µm. The initial temperature of the workpiece surface T_s was taken at 20˚C, with time-step set to be 10^{-8} s.

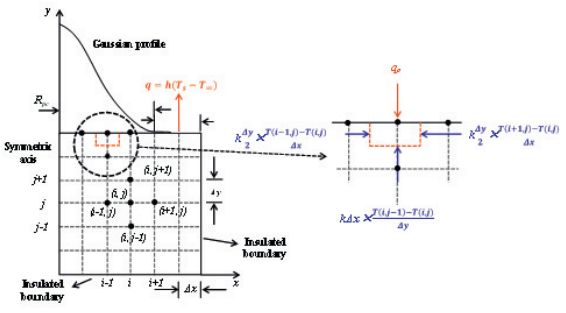

Figure 2 Incident Gaussian profile heat source and boundary conditions, including interior and top surface boundary nodes.

Conduction without heat generation was considered as the main mode of heat transfer between the plasma channel and the workpiece [8]. Heat loss from the top surface of the workpiece due to convection, as a result of the flow of fluid was also considered. Figure 2 illustrates the Gaussian heat distribution and interaction with the workpiece, and associated boundary conditions used for the analysis. The model was executed using MATLAB software.

The Fourier law of heat conduction used to drive this simulation, taking into account the boundary conditions of the system, is given by:

$$\frac{\partial^2 T}{\partial x^2} + \frac{\partial^2 T}{\partial y^2} = \frac{1}{\alpha}\frac{\partial T}{\partial t} \qquad (1)$$

Where T represents temperature, x and y are Cartesian coordinates which represent radius and depth of the crater, respectively, t is time, and α is thermal diffusivity of the material (m^2/s) and expressed as:

$$\alpha = \frac{k}{\rho\, c_p} \qquad (2)$$

Where k is thermal conductivity (W/m.K), ρ is density (kg/m^3) and c_p is the specific heat (J/kg.K). When the temperature of the workpiece material reaches a specific level during processing, some of material melts and is lost to the dielectric. However, some electrode material is deposited onto the workpiece surface and re-solidifies, and latent heat exchange is accompanied by a phase transition. Thus, thermal diffusivity, α', was taken into consideration in the simulation [9], given by:

$$\alpha' = \frac{k}{\rho(c_{p+L_m}/T_m)} \qquad (3)$$

Where L_m represents the latent heat of fusion (J/kg) and T_m is the melting temperature (K).

The energy transferred into the workpiece is characteristic of the shape and amount of energy presented to the workpiece surface. A Gaussian distribution heat source is widely accepted to approximate the plasma shape during the EDM process [10]. The Gaussian distribution of heat flux is given by:

$$(r) = q_0 e^{\left(-n\left(\frac{r}{R_{pc}}\right)^2\right)} \qquad (4)$$

For maximum heat flux q_o:

$$q_0 = \frac{4.57\ F_v\, V\, I}{\pi\, {R_{pc}}^2} \qquad (5)$$

Where q_o is heat flux (W/m^2), r is the radial distance from the

single spark centre line and R_{pc} is the plasma channel radius (both in metres), F_v is the fraction of total energy transferred to the workpiece, and I and V are current and voltage in A and V, respectively. The exponent (n) used in equation (4) relates to the flatness of Gaussian distribution.

There are inherent difficulties in measuring the plasma channel radius due to the small separation between the two electrodes in which the plasma occurs and the short pulse-on time of normally a few microseconds. However, researchers have proposed several empirical equations to calculate the plasma channel radius. In this work, the plasma channel radius was related to experimental crater measurements for a range of current and pulse-on times. Crater radii were measured using open source ImageJ software, with 30 measurements averaged, for each combination of current and pulse-on time [1]. After the pulse-on time ends, the cooling phase or pulse-off time begins, and the plasma channel collapses and dielectric fluid flows into the region where the plasma channel was located. At this point, molten material cools and re-solidifies, as a result of crater surface contact with the dielectric fluid and conduction into the substrate. Convection boundary conditions were applied on the surface through Newton's law:

$$q = h(T_s - T_\infty) \qquad (6)$$

Where h is the convection heat transfer coefficient ($W/m^2.K$), T_s is the surface temperature and T_∞ is the surrounding temperature (both in K). The heat transfer coefficient, h, is a function of fluid property, geometry, surface roughness and flow pattern. In the present work, uniform fluid flow over a flat plate, at constant velocity, was assumed.

3. Materials & Methods

The experimental work was carried using a die sinking EDM machine (Mitsubishi EA12V) with semi-sintered ($10\times20\times100$ mm^3) TiC tool electrode and a dielectric fluid (Shell Paraol 250). The workpiece material selected for experimentation was 304-SS, prepared into ($20\times20\times4$ mm^3) sections, polished to a mirror finish and washed with acetone prior to coating. Metallurgical analyses of the processed workpiece surfaces were performed using scanning electron microscopy (SEM) (FEI XL30 and Jeol 7100F) with energy dispersive X-ray spectroscopy (EDS) (Oxford Instruments, INCA). In order to measure the gap voltage and record voltage waveforms for all processing parameters during EDC, PC Oscilloscope (PicoScope 4224) and Differential Oscilloscope Probes (TA041) were used. Wear testing was performed under dry sliding conditions using a linear reciprocating ball-on-flat sliding method. No additional grinding was performed before wear testing (the as-deposited samples were simply cleaned with acetone). Based on preliminary experimentation, the wear test parameters chosen for this study were 10 N and 50 N normal loads, for 10,000 and 35,000 cycles, respectively, at a frequency of 2 Hz. The wear track length was kept at ~10 mm, and the experiments were conducted at room temperature. Each test were repeated three times using an alumina (Al_2O_3) ball of 9.525 mm diameter.

4. Results and discussion

4.1. Surface morphology and microstructure

The secondary electron (SE) image of Figure 3a shows the surface topography of the EDC TiC-Fe coating on 304-SS produced under conditions of 10 A current and 8 µs pulse-on time. Typical micro-cracks and voids can be seen, along with a crater based morphology typical of ED processing (Ra ~ 1.3 µm). EDS area analysis was performed on the TiC coated sample indicating a high amount of Ti (~ 39 wt.%), and hence TiC, was deposited on the substrate. Coating thicknesses were ~ 10 µm, but varied slightly depending on the discharge parameters.

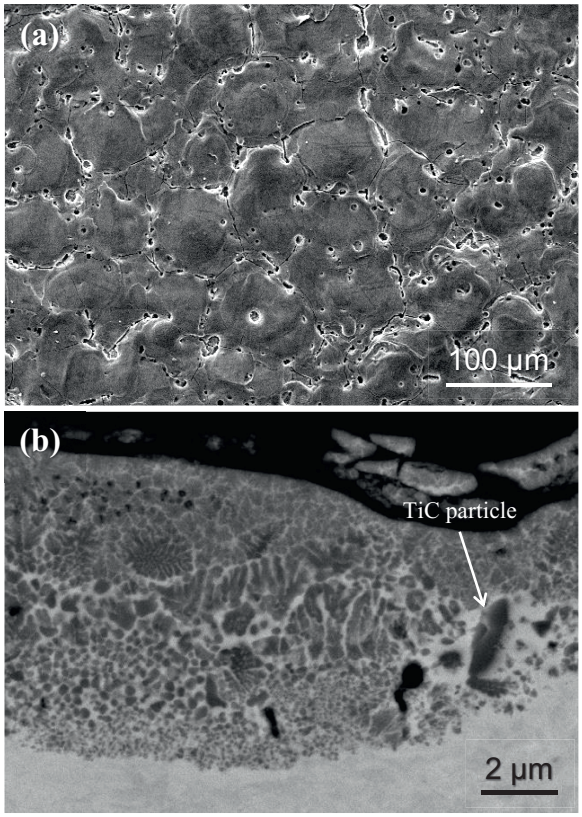

Figure 3. a) SE image of a TiC-Fe ED coating deposited at 10 A and 8 µs; b) Cross-sectional BSE image of a TiC-Fe ED coating on 304-SS.

Figure 3b shows the cross-sectional microstructure of an ED TiC-based coating on 304-SS. TiC appears dark in this backscattered electron (BSE) image due to the lower mean atomic number associated with Ti and C compared to Fe. The metal matrix composite (MMC or cermet) nature of the coating can be clearly seen, comprising a complicated,

intermixed microstructure which varies significantly based on depth into the coating. The presence of substrate material (Fe) within the coating reveals the extent of intermixing of substrate and deposited material [1, 2]. Large, presumably unmelted particles of TiC present (Fig. 3b, arrowed) also show the complexity of the formation mechanism, whereby material may move into the coating during processing directly from the sacrificial electrode without fully melting.

Figure 4 presents XRD patterns of the as-polished 304-SS substrate and the ED TiC-based coating. The substrate is mainly composed of γ austenite (fcc) and some α` martensite (bcc). The martensite phase in 304-SS is likely to have developed after cold working. The surfaces prepared with the TiC electrode contained the TiC phase, along with evidence of austenite and martensite. Small peaks attributable to Fe_3C, Cr_3C_2 and carbon were also detected.

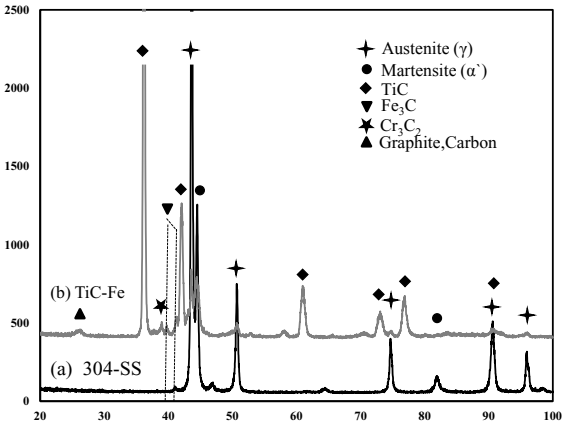

Figure 4 XRD patterns of the a) as-polished 304-SS substrate and b) TiC-Fe cermet coating.

4.2. Fraction of energy transfer and model validation

Figure 5 presents a comparison of the energy transferred to the workpiece during EDC processing, as predicted by the model proposed above, compared to that reported by Singh [11] and Shabgard *et al.* [12], as a function of increasing current and pulse-on time. The mean gap voltage was set at ~320 V, whilst the mean discharge voltage varied as a function of pulse-on time, measured at 30 V for the 2-16 µs pulse-on time, decreasing to 23 V and 18 V for the 32 µs and 64 µs test, respectively. The energy distribution ratio into the workpiece showed variation between 17% and 23% with increasing current, at a fixed pulse on-time of 8 µs. However, increasing pulse-on time, for a fixed current of 10 A, led to a significant increase in the amount of energy transferred into the workpiece from 7% to 53%. The tendency for increased fraction of energy transfer with increasing pulse-on time was attributed to the development of a steady heat source. Overall, the values of the F_v are in good agreement with previous reports, but are slightly higher which may be attributed to the ED-coating mechanism of alloying and replacement of electrode material with workpiece material, rather than removal, as in EDM processing. It is also acknowledged that the current work uses an anode workpiece, as distinct from a cathodic workpiece used in the work referenced. The disparity in energy balance between polarity types may contribute the difference in results shown (Figure 5).

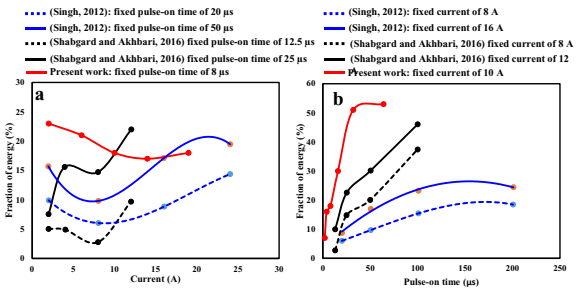

Figure 5 Fraction of energy transferred to the workpiece during EDC processing, compared to EDM process literature [11, 12].

4.3. Heat distribution

Figure 6 presents a simulation of temperature distribution into the workpiece due to a single spark event, under conditions of 10 A current and 8 µs pulse-on time. The dotted white line represents temperature distribution along the top surface of the crater, in a radial direction from the centre line of the discharge. The highest temperature was found at the centre and gradually decreased with increasing distance from the origin. This behaviour is strongly related to the Gaussian distribution of the heat flux equation. The maximum value of energy is at the crater centre where the radius value is zero. The dashed white line represents the boundary of melted material, obtained by comparing the temperature of each node with the melting temperature of 304-SS.

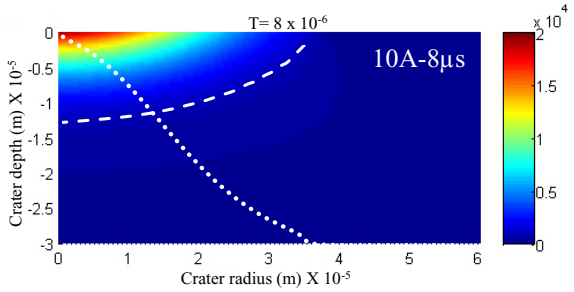

Figure 6 MATLAB simulation showing heat distribution into the workpiece at 10 A current and 8 µs pulse-on time; along with the temperature distribution along the top surface of the crater (dotted white line) and the boundary of molten material (dashed white line).

4.4. Cooling phase and coating microstructural development

Figure 7 depicts the microstructure generated within a crater processed under conditions of 10 A current and 8 µs pulse-on time (cf. Figure 3b), along with temperature plots

along the crater depth as a function of the cooling time, with each curve representing a node located at different depths (1 µm pitch) into the centre of the crater. The first point represents the upper crater surface, or coating/oil-flow interface, and the last point represents the melt/solid interface within a single crater.

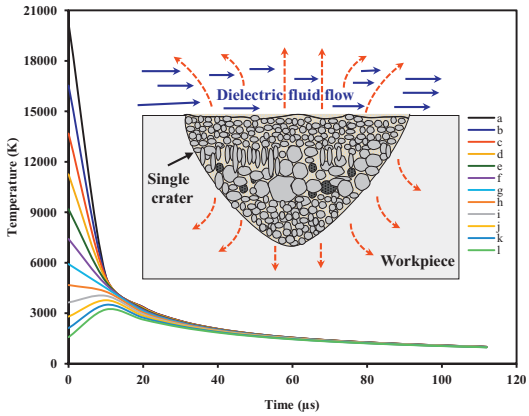

Figure 7 Cooling profiles with time (pulse-off) for different depths into a crater

It is noted that the temperature of the near surface molten material decreases sharply from ~ 20,000 K on the surface to ~ 4,000 K within 10 µs of the pulse-off time, followed by a lower cooling rate. This behaviour of rapid initial cooling is likely to be imposed by the flowing oil and governed by a convection mode within the dielectric fluid, whilst an initial slight temperature increase combined with relatively slower cooling rates in the vicinity of the melt/solid (crater/substrate) interface (~ 3 µm) from the bottom of the crater, is governed by conduction heat transfer into the substrate. This results in a banded microstructure within the crater depth, which is defined by the competing heat transfer processes. Hence, it is evident that the cooling phase of a single crater has two distinct stages, with rapid non-uniform cooling within the first (~10–20 µs) leading up to the onset of TiC crystallisation, followed by a second more uniform stage of heat loss, up to ~100 µs, leading up to the onset of Fe matrix solidification

4.5. Specific wear rates and wear scar characterisation

The specific wear rates of the as-polished 304-SS substrate, an EDM Cu machined surface and an EDC TiC-Fe coating are presented in Figure 8. The TiC-based cermet coating provides for significant tribological improvement, under both loading conditions 10 N and 50 N, with approximately a two order of magnitude lower specific wear rate compared to the as-polished substrate. Interestingly, the simple EDM machined surface yielded over an order of magnitude reduction in specific wear rate at 10 N compared, to the 304-SS substrate only. This improvement was not seen at the higher load of 50 N. The reduction in wear rate for the TiC-based coating compared to the conventional EDM Cu machined surface is ~1 order of magnitude lower at 10 N and ~2 orders of magnitude at 50 N.

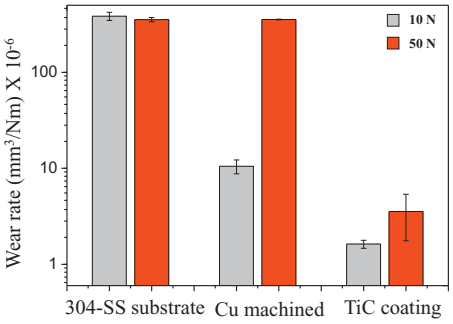

Figure 8 Specific wear rates (logarithmic scale) for samples based on 304-SS substrates (as-polished substrate; EDM Cu machined surface; and EDC TiC-Fe coating) under loads of 10 N and 50 N.

Figure 9 presents SE images of wear scar features on the three sample types, under conditions of 10 N and 50 N loading. Wear tracks on the TiC coating under low loads showed uniform, smooth surfaces. Initial cracks and voids associated with the EDC process could also be seen (Figure 9e). At 50 N load, the wear tracks showed evidence of fracture and pull-out of material (Figure 9f), with new developed cracks distinct from initial EDC cracks also seen.

The as-polished substrate and the EDM Cu-machined surfaces generally showed similar wear track morphologies, except at 10 N on the Cu-machined surface, which showed sharp abrasive grooves and delaminated regions, possibly indicating an adhesive mechanism. Further, some cracks and voids associated with the initial EDM process were found (Figure 9c). Conversely, at the high loading condition 50 N, the surface exhibited more severe wear, with the dominance of adhesive wear along with some abrasive wear (Figure 9d).

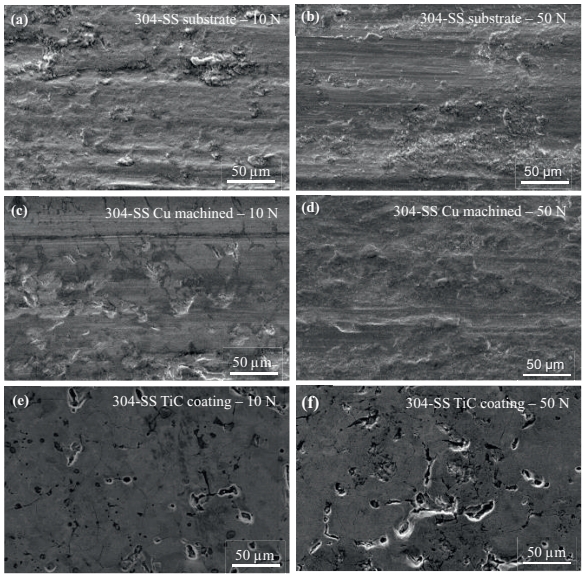

Figure 9 High magnification SE images of the wear tracks under conditions of 10 and 50 N load, for as-polished 304-SS, an EDM Cu reference sample, and an EDC TiC-Fe cermet coating.

The as-polished 304-SS showed the same wear morphology, under both loading conditions of 10 and 50 N, exhibiting evidence of a severe wear regime with wear debris and delamination (Figures 9a,b). Given the stark improvement in wear rates for the TiC-Fe coating, under both loading conditions, it is clear that the incorporation of TiC into the coating results in a milder wear regime, which avoids any adhesive wear mechanism, and generally avoids the tendency for fracture.

Figure 10 shows the coefficient of friction (CoF) yielded by wear tests on the as-polished substrate, the Cu machined surface and a TiC-based coating, at 10 and 50 N load. The TiC-Fe coatings yielded the lowest CoF, for all samples and loads. The cermet coating on 304-SS exhibited very low friction coefficients at 10 N load (Figure 10a, gray line). At 50 N load the CoF exhibited a gradual increase throughout the entire duration of the test (Figure 10b, gray line).

The CoF of the as-polished 304-SS at 10 N showed an initial rapid increase associated with an increase in contact area, followed by steady state friction at an average of ~ 0.8, although with a more erratic and high friction value after the initial run-in period (Figure 10a, black line). At 50 N load the CoF of the 304-SS showed a steady increase to reach a value of ~1.2 at the end of the test (Figure 10b, black line). The friction coefficients of the EDM Cu machined sample, at 10 and 50 N load, showed similar patterns to that of the substrate (Figures 10a,b, red lines).

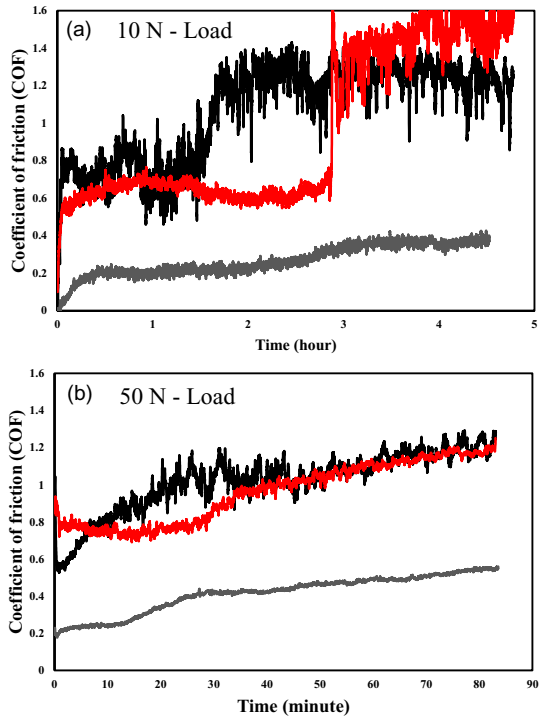

Figure 10 CoF obtained with a) 10 N load and b) 50 N load for the as-polished 304-SS substrate (black line), EDM Cu machined (red line) and TiC-Fe coating (gray line).

5. Conclusion

TiC can be deposited successfully on 304-SS using the EDC technique, yielding effectively a metal matrix TiC-Fe composite, with the development of complex, banded, fine-grained microstructures, due to intermixing of substrate with deposited material, mediated by different cooling rates across the coating. A 2D transient heat transfer model was developed, which predicted that the amount of energy transferred to the workpiece varied between 17% and 23% for increasing current from 2 to 19 A, at a fixed pulse-on time 8 µs; and between 7% and 53% for increasing pulse-on time from 2 to 64 µs, at a fixed current of 10 A. A TiC-Fe coating on 304-SS yielded a wear rate, under dry sliding conditions, between one and two orders of magnitude lower than that of the Cu EDM'd surface and substrate, respectively.

Acknowledgements

Samer J. Algodi thanks the Ministry of Higher Education & Scientific Research in Iraq for funding support. A.T. Clare would like to acknowledge funding from the Engineering and Physical Sciences Research Council (EPSRC) [EP/L017547/1]. In addition, the authors acknowledge the kind support of Mr Iwasaki of Mitsubishi Electric Nagoya.

References

1. Algodi, S.J., et al., Electrical discharge coating of nanostructured TiC-Fe cermets on 304 stainless steel. Surface and Coatings Technology, 2016. 307: p. 639-649.
2. Murray, J.W., et al., Formation mechanism of electrical discharge TiC-Fe composite coatings. Journal of Materials Processing Technology, 2017. 243: p. 143-151.
3. Singh, S. and A. Bhardwaj, Review to EDM by using water and powder-mixed dielectric fluid. Journal of Minerals and Materials Characterization and Engineering, 2011. 10(02): p. 199.
4. Singh, H. and D. Shukla, Optimizing electric discharge machining parameters for tungsten-carbide utilizing thermo-mathematical modelling. International Journal of Thermal Sciences, 2012. 59: p. 161-175.
5. Tan, P. and S. Yeo, Modelling of overlapping craters in micro-electrical discharge machining. Journal of Physics D: Applied Physics, 2008. 41(20): p. 205302.
6. Yeo, S., W. Kurnia, and P. Tan, Critical assessment and numerical comparison of electro-thermal models in EDM. Journal of materials processing technology, 2008. 203(1): p. 241-251.
7. DiBitonto, D.D., et al., Theoretical models of the electrical discharge machining process. I. A simple cathode erosion model. Journal of Applied Physics, 1989. 66(9): p. 4095-4103.
8. Joshi, S. and S. Pande, Thermo-physical modeling of die-sinking EDM process. Journal of manufacturing processes, 2010. 12(1): p. 45-56.
9. Zhang, Y., et al., A novel method of determining energy distribution and plasma diameter of EDM. International Journal of Heat and Mass Transfer, 2014. 75: p. 425-432.
10. Das, S., M. Klotz, and F. Klocke, EDM simulation: finite element-based calculation of deformation, microstructure and residual stresses. Journal of Materials Processing Technology, 2003. 142(2): p. 434-451.
11. Singh, H., Experimental study of distribution of energy during EDM process for utilization in thermal models. International Journal of Heat and Mass Transfer, 2012. 55(19): p. 5053-5064.
12. Shabgard, M. and S. Akhbari, An inverse heat conduction method to determine the energy transferred to the workpiece in EDM process. The International Journal of Advanced Manufacturing Technology, 2016. 83(5-8): p. 1037-1045.